CIRP Journal of Manufacturing Science and Technology 66 (2026) 70–85

Contents lists available at ScienceDirect

CIRP Journal of Manufacturing Science and Technology

journal homepage: www.elsevier.com/locate/cirpj

Full-length article

A predictive thermomechanical model for peck drilling

Mattia Pelosin [a,*], Alessandro Moramarco [b], Luca Bernini [a,b], Paolo Albertelli [a,b], Tommaso Lucchini [c]

[a] Politecnico di Milano, Department of Mechanical Engineering, via La Masa, 1, Milan, 20156, Lombardy, Italy
[b] MUSP Macchine Utensili Sistemi di Produzione, strada della Torre della Razza, Piacenza, 29122, Emilia-Romagna, Italy
[c] Politecnico di Milano, Department of Energy, via Lambruschini, 4, Milan, 20156, Lombardy, Italy

ARTICLE INFO

Keywords:
Peck drilling
Thermomechanical model
Thermal experimental analysis
FVM modelling
Analytic thermal modelling

ABSTRACT

Drilling processes produce significant heat due to friction and material deformation, which can lead to tool wear, surface damage, and residual stress in the workpiece. To mitigate these effects, the peck drilling strategy was developed, incorporating periodic tool retractions to lower peak cutting temperatures and enhance chip evacuation. Consequently, accurate temperature distribution predictions are essential to improve drilling performance and ensure part quality. Few works in the literature focused on peck drilling operations, whose success is mainly influenced by the mitigation of the cutting temperature. To fill this gap, this study introduces a comprehensive predictive framework for evaluating cutting forces and temperatures in peck drilling. It combines an analytical force model with two distinct thermal analysis methods: an analytical technique and a Finite Volume Method (FVM) simulation. A novel oblique cutting model, grounded in Oxley's machining theory and incorporating the Johnson–Cook material model, is proposed. The analytical thermal approach extends the infinitesimal point-source method to represent transient heat conduction in finite media, while the FVM simulation numerically models heat transfer and material removal dynamics. To validate the framework, an experimental campaign was conducted under various cutting conditions. Results demonstrate the model's capability to reliably estimate cutting forces and temperature distributions across a wide range of parameters. The average prediction errors were 4.66% for cutting power, 7.45% for cutting forces, and for maximum temperature, 8% with the FVM and 11.64% using the analytical method. The developed framework lays the groundwork for future investigations into the impact of lubrication strategies on peck drilling.

1. Introduction

Drilling is one of the most used metal-cutting operations in the manufacturing industry. Even though it is a mature technology, it requires specific attention to achieve optimal results. In fact, during metal cutting, significant heat is generated due to friction between the cutting tool and the workpiece, as well as the plastic deformation of the material forming chips. High cutting temperatures have detrimental effects on both the cutting tool and the workpiece [1]. Excessive heat generation causes rapid wear for the drill bit, shortening its lifespan, and may result in plastic deformation of the cutting edges if the tool lacks sufficient hot-hardness and strength [2]. Thermal shocks may lead to flaking and fracturing of the cutting edges [3], while the formation of built-up edges further degrades the cutting performance [4]. Excessive heat may also lead to dimensional inaccuracies due to thermal distortion and expansion–contraction during and after machining [5]. The surface may suffer damage through oxidation, rapid corrosion, or burning, while residual tensile stresses and micro-cracks may form on the surface or subsurface, further compromising its integrity [6,7].

The temperature generated during machining is influenced by various factors, such as the materials of the tool and workpiece, cutting parameters, and the type and application method of cutting fluids [8]. Drilling strategy also plays an important role. Indeed, peck drilling is often adopted to mitigate the cited problems [9,10]. It consists of splitting the total drilling length into sequential dives, divided by a short period in which the drill returns to the workpiece surface [11]. This strategy helps to keep the cutting temperature under control and to evacuate the chip from the hole. Eltaggaz et al. [11] compared continuous and peck drilling of Ti-6Al-4V in terms of tool life, surface roughness, thrust force, torque, and burr formation. The facilitated chip removal of peck drilling allowed for lower thrust force and torque and reduced the flank wear. Peck drilling produced slightly higher surface roughness compared to continuous drilling; the authors suggest

* Corresponding author.
E-mail addresses: mattia.pelosin@polimi.it (M. Pelosin), alessandro.moramarco@musp.net (A. Moramarco), luca1.bernini@polimi.it (L. Bernini), paolo.albertelli@polimi.it (P. Albertelli), tommaso.lucchini@polimi.it (T. Lucchini).

https://doi.org/10.1016/j.cirpj.2026.02.002
Received 13 August 2025; Received in revised form 4 February 2026; Accepted 6 February 2026
Available online 11 February 2026

this occurs because, during peck drilling, when the drill periodically retracts, the flood coolant can wash debris and chips back into the hole. When the drill re-enters, it can cause these particles to rub against the hole wall, creating additional surface damage and increasing roughness. Pervaiz et al.'s [12] investigation of peck drilling hole quality in aluminium 6061 revealed that each new drilling step significantly impacts the surface roughness of previously drilled sections. Their work demonstrates that both step length and the total number of steps are critical factors controlling surface quality in peck drilling operations. Ravisubramanian et al. [13] proved that peck drilling strategy enabled the production of large aspect-ratio micro-holes without drill breakage in aluminium 6061-T6. By drilling through 3 mm thick plates, the researchers achieved micro-holes with an aspect ratio of 6:1, demonstrating the effectiveness of this approach for challenging deep-hole applications. Compared to direct drilling, thrust force and drilling torque in peck drilling are observed to be lower.

It follows that studying temperature distribution and maximum temperature in metal cutting is crucial for determining optimal cutting parameters. Despite its importance, direct measurement of temperature at the tool-chip interface during metal cutting is unfeasible due to physical inaccessibility. Temperature is hence often estimated indirectly through mathematical models, simulations, or measurement of related parameters [14]. The primary factors causing temperature increase are the dissipation of the plastic energy and the friction between the chip and the tool, which directly determine the cutting forces. An estimation of the temperature must hence start from the modelling of the solid mechanics characteristics of drilling cutting [15].

The prediction of machining forces in drilling has been extensively studied using empirical, mechanistic, and Finite Element Methods (FEM). Empirical models were initially developed to investigate the relationships between thrust force, torque, and the drilling parameters [16,17]. While these models provided valuable insights, they were limited by their reliance on regression-based fitting and lacked physical understanding of the process. Mechanistic approaches subsequently improved upon empirical models by incorporating detailed process kinematics and assuming that cutting forces are proportional to the uncut chip area or chip load [18], all of which are grounded in the foundational model proposed by Oxley [19]. This method requires fewer calibration experiments and offers better accuracy across a broader range of conditions because of its background in process physics. For instance, Chandrasekharan et al. [20] utilised a mechanistic approach to model cutting forces and predict thrust and torque in drilling processes, specifically addressing the dynamics of Fiber-Reinforced Composite Materials (FRCM). Their model accounted for parameters such as chip load, chip thickness, and cutting angles, which remain consistent across metals and FRCM. The finite element method directly simulated the 3D chip deformation and breakage [18]. Despite being computationally intensive and time-consuming, FEM approaches are the most accurate and require experimental data only for validation purposes.

Also, the cutting temperature evolution was directly investigated in the literature with the different approaches just described. Analytical methods predict temperature using process parameters or measurements from adjacent areas, such as the chip or workpiece. Despite their computational efficiency, these methods require simplifying assumptions, which introduce errors, and involve high mathematical complexity [21]. Empirical methods involve experiments to model the relationships between input parameters (e.g., cutting speed, feed rate) and outputs like cutting forces or temperatures. These methods are constrained by the need for experimental data and assumptions [21]. Numerical methods, such as FEM, simulate the thermal field in machining with fewer assumptions than analytical methods. While highly accurate, these approaches demand substantial computational resources and extensive experimental inputs [21].

Strenkowski et al. [22] exemplified this by developing a finite element model for drilling, representing the drill cutting lips as a series of oblique sections. Using an analytical model for oblique cutting, they calculated three-dimensional cutting forces at each section to predict thrust and torque under various operating conditions. Their model was validated both through drilling experiments on AISI 1020 steel using high-speed steel drills with different diameters and feed rates and by comparing torque predictions with published data. These results confirmed the reliability of FEM in predicting both thrust and torque for drilling applications. Patne et al. [23] combined analytical, numerical, and empirical methods to estimate temperatures during the drilling of titanium alloys. After determining heat partitioning analytically, they used FEM simulations to model the thermal field and validated results with infrared (IR) camera measurements and thermocouples embedded in the drill. Their findings highlighted the relationship between cutting speed, feed rate, and temperature distribution in the workpiece. Segurajauregui et al. [24] focused on quantifying heat transfer during drilling operations. They found that higher cutting speeds reduced the heat transferred to the workpiece, while lower feed rates increased it. Using FEM simulations and IR measurements, they predicted distortions caused by heat input during machining. Fleischer et al. [25] developed a mathematical model to simulate the input heat flux for FEM-based distortion analysis during machining with Minimum Quantity Lubrication. They showed that surface heat flux depends linearly on cutting speed and tool diameter, while its relationship with feed rate follows a polynomial or exponential trend. Experiments with thermocouples revealed that heat generation varies significantly with tool wear and cutting parameters. Kumar et al. presented a CFD-FEM model for simulating the cryogenic drilling of Titanium alloys [26] to investigate the temperature distribution under various cooling strategies.

Nevertheless, no research provided insights into the mechanics of peck drilling and the associated thermal analysis. With this scope, a predictive approach for the estimation of cutting forces and temperatures for peck drilling operation is proposed, based on the integration of an analytic model for the forces estimation with two different types of thermal analysis (Section 2.1). For this purpose, the orthogonal mechanistic model of Lalwani et al. [27] for orthogonal cutting is extended to oblique cutting to study the phenomenology of the drilling process. Lalwani et al. modified Oxley's predictive model [19] to include the Johnson and Cook flow stress material model. This provided an analytical framework for chip formation and cutting force determination in orthogonal cutting, incorporating assumptions about the shear zones, strain rates, and the effects of temperature on flow stress. Since drilling is an oblique cutting process, we introduced a third force component to extend Lalwani's model for peck drilling, drawing on the works of Minukhin [28] and Altintas [29] (Section 2.1.1). Furthermore, two alternative approaches are conceived to estimate the workpiece temperature evolution. An analytic model (Section 2.1.2) is conceived based on the heat solution for a conical moving heat source, starting from the work by Shi et al. [30]. The solution was extended from the hypothesis of an infinite to a semi-infinite medium by mirroring heat sources to analyse a workpiece, with non-negligible boundary effects. A thermal Finite Volume (FV) analysis is also carried out and described in Section 2.1.3. Finite Volume differs from Finite Element in the discretisation methodology adopted. The use of FV in the machining sector is, up to now, limited to the study of the fluid dynamics of the working fluid in various processes [31–33], while its application to model temperature evolution in the drilling process is a novelty in the literature. A side to the advantages deriving from a 3D analysis, which are comparable to the FEM modelling, this discretisation methodology is at the base of Computational Fluid Dynamics, hence it is interesting for integrating the effect of the lubrication strategy in a coupled thermal simulation. This potentiality is possible since the simulations are performed in OpenFOAM, an open-source software that keeps both solid and fluid dynamic solvers. A similar simulation technique was previously proposed by the authors for cryogenic orthogonal cutting [34].

The developed model is specifically designed for applications where global machining parameters and workpiece thermal response are the

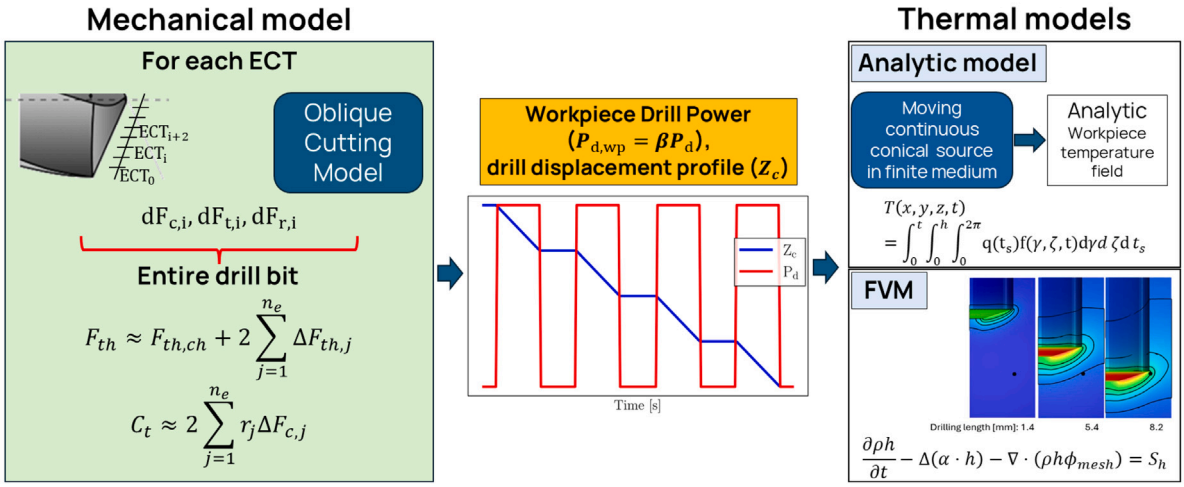

Fig. 1. Overview of the numerical methodology.

primary concern, rather than detailed chip morphology. Finite Element (FE) modelling can accurately capture chip formation mechanisms [35]; however, this approach inherently requires extremely fine spatial and temporal resolution. As a consequence, simulating a peck drilling process through FEM would demand modelling physical times on the order of tens of seconds and a computational domain several orders of magnitude larger than the chip itself. These requirements render full FE simulation of multi-peck drilling cycles computationally prohibitive, making the approach impractical for engineering design and process optimisation studies. In contrast, the methodology proposed in this work achieves a similar level of insight at a fraction of the computational cost when the objective is to investigate temperature evolution in the workpiece and the influence of process parameters. The FVM-based simulation requires approximately 3000 s per processor, while the analytical model completes in about 60 s. This efficiency enables parametric studies, process optimisation, and rapid evaluation of multiple drilling strategies, capabilities essential for industrial implementation.

The developed numerical methodology is supported by an experimental campaign for validation purposes, varying both the operating conditions and the drilling-bit (see Section 2.2.2). The proposed model proved to be reliable in a wide range of cutting velocities and feed rates, both for the forces and the temperature estimation (Section 3). Conclusions are drawn in Section 4.

2. Materials and methods

This section describes the conceived simulation framework (Section 2.1) and the experimental apparatus conceived for its validation (Section 2.2). The modification made to the Lalwani model [27] made to study oblique cutting and the analytic and finite volume thermal models are described. Followed by the description of the experimental setup and the data acquisition system.

2.1. Numerical model

Thermal power originates from the dissipation of plastic deformation energy and friction between the chip and tool, necessitating a mechanistic model for its estimation. This thermal power, proportional to the mechanical cutting power, serves as input to thermal models for temperature prediction. The proposed methodology, illustrated in Fig. 1, follows this sequence: (1) the mechanistic model for oblique cutting computes cutting forces and power, (2) the resulting cutting power is scaled by a partition coefficient and applied to the thermal models with a time-varying profile consistent with the peck-drilling strategy to estimate workpiece temperature.

The modelling framework relies on the following key assumptions, detailed in subsequent sections:

- Drilling is modelled as an oblique cutting process;
- Cutting forces and power are assumed constant during the active (engagement) phases of each peck;
- Heat transfer to the workpiece is represented as a fraction of the total cutting power, determined by the partition coefficient;
- The peck-drilling strategy is incorporated through time-dependent thermal power and drill displacement inputs to the thermal model;
- The analytical thermal model treats the workpiece as a continuous solid throughout the process, neglecting material removal. Consequently, heat propagates bidirectionally, both downward into the uncut material and upward through previously machined regions;
- The heat generated by the friction between the drill bit and the hole wall is neglected.

The mechanistic model is inherently steady-state and thus does not directly account for the peck drilling strategy. This assumption does not limit the validity of the modelling strategy, since mechanical transients are very fast and the cutting power reaches steady-state almost immediately during the active phases of the pecks. This behaviour is visible in the measured forces and power temporal evolution (Fig. 10), which exhibit a square wave profile, aside from secondary oscillations. The power input is active and equal to the cutting power scaled by the partition coefficient during the engagement phase of each peck and null during the retraction periods.

2.1.1. Mechanical model

Cutting processes can be distinguished between orthogonal and oblique depending on the angle at which the cutting tool approaches the workpiece. While in orthogonal cutting the cutting edge of the tool is orthogonal to the cutting speed (V), in oblique cutting the cutting edge falls at an arbitrary angle to the cutting speed [29]. Indeed, drilling falls in this second category. Because drilling is inherently a three-dimensional machining process, the conditions vary along the cutting edge. As a result, an oblique cutting model cannot be directly applied, since the effective cutting angles change along the cutting lip. However, the cutting edge can be decomposed into infinitesimal oblique cutting elements in which the tool geometry and cutting angles can be considered locally constant, making the application of oblique cutting theory mathematically valid. The global cutting forces can then be obtained by integrating the infinitesimal forces over the cutting edge. In practice, the cutting edge is discretised into a finite number of Elementary Cutting Tools (ECTs), and the oblique cutting model is

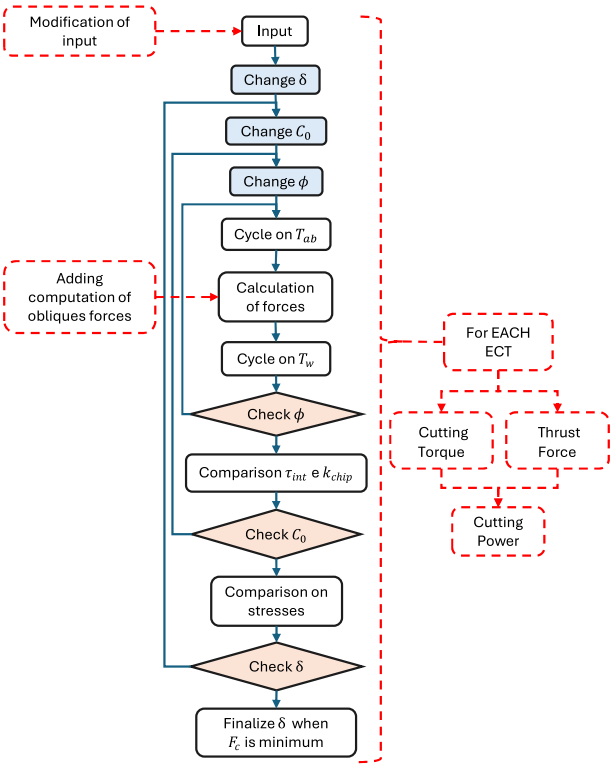

Fig. 2. Iterative algorithm of the mechanical model. Red dashed blocks are extensions necessary for oblique cutting [27].

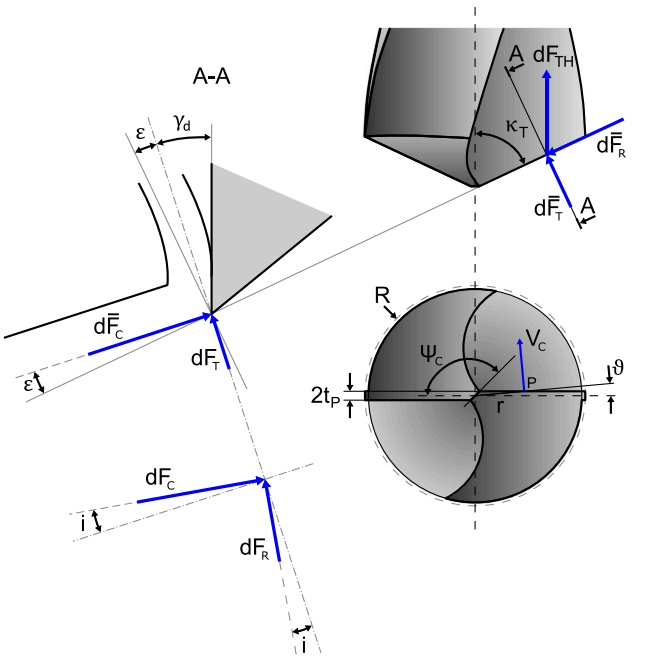

Fig. 3. Geometry and angles associated with the drill bit. Cutting forces generated during drilling.

evaluated for each of them. Finally, by performing a global force and moment balance along the drilling edge, the overall drilling forces and power consumption can be estimated. This approach was validated in literature both for drilling [23,36] and milling [37,38] operations.

A mechanistic model was developed to analyse peck drilling by extending the predictive machining framework for orthogonal cutting proposed by Lalwani et al. [27] to an oblique cutting configuration. Predictive machining models offer a simplified yet physically grounded representation of the stress and strain fields during cutting. They are based on the Oxley theory [19], a thick shear zone model for cutting which includes the effects of strain hardening, strain rate and temperature on the material properties. The deformation of the chip is assumed to occur in the Primary Shear Zone (PSZ), which runs parallel and equidistant to the primary shear plane, defined as the plane with the maximum shear stresses. A secondary shear zone exists at the tool-chip interface, which is assumed to be of constant thickness. Oxley's theory employs a power law formulation for the flow stress field. However, this formulation was applied only to a limited number of materials, thereby limiting its applicability. Lalwani [27] modified this theory by replacing the Johnson Cook flow stress model (Eq. (1)):

$$\sigma = (A + B\varepsilon^n)\left(1 + C\ln\frac{\dot{\varepsilon}}{\dot{\varepsilon}_0}\right)\left(1 - \left(\frac{T - T_a}{T_m - T_a}\right)^m\right), \tag{1}$$

to the power law. Where σ is the plastic flow field, ε is the strain, $\dot{\varepsilon}$ is the strain rate, T_a is the ambient temperature, T_m is the melting points and A, B, C, n, m are experimental coefficients. In this way, the effects of the material temperature and strain rate on the flow stress are considered. Furthermore, a large database exists for this flow stress model, making it applicable to a wider range of materials.

The numerical model employs an iterative procedure that calculates the stress state within the primary and secondary shear zones as a function of: (a) the primary shear angle (ϕ), which defines the orientation of the primary shear plane; (b) strain-rate constant C_0 at shear zone, hence the ratio of shear plane length to thickness of the primary shear zone and (c) strain-rate constant δ at tool–chip interface, hence the ratio of the thickness of secondary shear zone to chip thickness.

Convergence is achieved when the applied forces are in equilibrium with the internal stress state of the material, and the condition corresponding to the minimum energy required for the creation of the chip is therefore achieved. In particular, the optimal value of the three parameters is achieved when:

- ϕ is such that the shear stress τ_{int}, determined from the component of the resultant force parallel to the tool–chip interface, matches the shear flow stress k_{chip} in the chip material at the interface. Where:

$$\tau_{int} = \frac{F}{hw},\ k_{\text{chip}} = \frac{1}{\sqrt{3}}\left(A + B\varepsilon_{\text{int}}^n\right)\left(1 + C\ln\frac{\dot{\varepsilon}_{\text{int}}}{\dot{\varepsilon}_0}\right)\left(1 - \left(\frac{T_{\text{int}} - T_w}{T_m - T_w}\right)^m\right); \tag{2}$$

- C_0 guarantees that the normal stress at the tool-chip interface, calculated to the force component normal to the tool-chip interface, matches the inner normal flow stress;
- δ corresponds to the minimum cutting force condition.

With reference to Fig. 3, the following trigonometric analysis has been performed to extend this model to oblique cutting.

A web angle ϑ is introduced, generated between the cutting lip and the radial line connecting the drill bit centre to a generic point P of the cutting lip [28,29], defined as:

$$\sin\vartheta = \frac{w}{r}, \tag{3}$$

where w is the half-web thickness, and r the generic radial coordinate of point P.

The helix angle β_r, computed at point P, is a function of the nominal helix angle β_0 (at $r = R$) as follows:

$$\tan\beta_r = \frac{r}{R}\tan\beta, \tag{4}$$

where R is the drill bit radius [28]. Two oblique angles can be computed starting from ϑ and the drill bit half taper angle κ_t. The inclination angle i and the reference angle ε are thus defined as [28,29]:

$$\sin i = \sin\vartheta \sin\kappa_t,$$
$$\tan\varepsilon = \tan\vartheta \cos\kappa_t. \tag{5}$$

It is thus possible to compute the uncut chip thickness t_1 through Eq. (6) [28], based on the feed per revolution c, which is an input parameter of the model:

$$t_1 = \frac{c}{2}\sin\kappa_t \cos\varepsilon. \tag{6}$$

The dynamic rake angle, a fundamental angle for oblique cutting, is introduced [28,29]:

$$\tan\gamma_d = \frac{\tan\beta_r}{\sin\kappa_t}\left(\cos\vartheta + \sin\vartheta\tan\vartheta\cos^2\kappa_t\right) - \tan\vartheta\cos\kappa_t. \tag{7}$$

For low feed drilling applications, the dynamic rake angle can be simplified and assumed equal to the static rake angle.

Three infinitesimal cutting forces components are generated at the infinitesimal cutting lip at point P. Such components are aligned to the tangential, radial and cutting directions of a frame aligned with the infinitesimal cutting lips, and are identified with an overline in Fig. 3. Their expressions are shown in Eq. (8) and they are function of the reference ε and inclination i angles reported in Fig. 3 [28]:

$$\begin{aligned} \mathrm{d}\overline{F}_t &= \mathrm{d}F_t\cos\varepsilon - \mathrm{d}F_c\sin\varepsilon,\\ \mathrm{d}\overline{F}_r &= \mathrm{d}F_r\cos i - \mathrm{d}F_c\sin i,\\ \mathrm{d}\overline{F}_c &= \mathrm{d}F_c\cos i - \mathrm{d}F_r\sin i. \end{aligned} \tag{8}$$

The cutting $\mathrm{d}F_c$ and $\mathrm{d}F_t$ components of forces are assumed to be independent of the inclination angle i. This assumption was widely adopted in literature starting from experimental observations in [39]. The authors observed that for a given normal rake angle, these forces were very nearly independent of the inclination angle [40]. Such an assumption found applications in different works, such as [41], which made the basis of several later developed methods. Indeed, the cutting and tangential forces can be computed with the orthogonal cutting formulation, following Lalwani et al.'s work [27] (and the central part of Fig. 2). The radial force component $\mathrm{d}F_r$, the only one missing, is derived from $\mathrm{d}F_c$, $\mathrm{d}F_t$, γ_d and the friction angle β_a [28]:

$$\mathrm{d}F_r = \sqrt{\mathrm{d}F_c^2 + \mathrm{d}F_t^2}\sin\beta_a\cos\gamma_d\tan i. \tag{9}$$

According to Stabler's rule [42], the chip flow angle η was considered to be equal to the inclination angle i. Stabler's rule is widely adopted and agreed upon in the literature of oblique cutting processes [40]. Nevertheless, some extensions or alternative formulations may be adopted in case of different workpiece materials [43] and cutting conditions (e.g., cutting speed) [43,44], or taking into consideration the normal rake angle [45]. Finally, the thrust force generated on the infinitesimal element of the cutting lip is:

$$\mathrm{d}F_{th,lip} = \mathrm{d}\overline{F}_t\sin\kappa_t - \mathrm{d}\overline{F}_r\cos\kappa_t. \tag{10}$$

Being the above quantities defined at a generic point P, they are all functions of the radial distance r from the drill bit centre. Indeed, cutting angles and the cutting velocities change moving along the lip, since the peripheral velocity grows with the radius and the lip geometry changes. It follows that the forces distribution is not uniform, and to correctly describe this behaviour is necessary to split the cutting lip into n_e finite parts named Elemental Cutting Tools (ECTs). The oblique cutting model is then applied to each ECT. The global quantities are hence retrieved with a global force balance. The number of ECTs considered derives from a trade-off between accuracy and computational efficiency (in this paper, the cutting lip was discretised in $n_e = 8$ ECTs).

The total thrust force F_{th} generated on the tool accounts for two terms: the lip contribution, described above, and the chisel contribution. The chisel contribution is devoted to material indentation and can be defined as follows [29]:

$$F_{th,ch} = A_{ch}H_b, \tag{11}$$

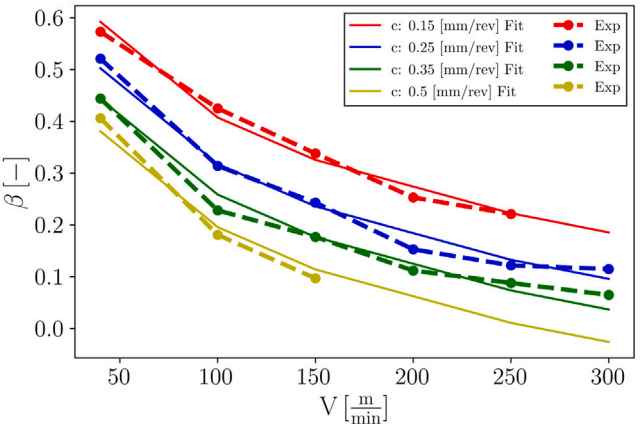

Fig. 4. Dependency of partition coefficient from cutting velocity and feed rate.

where H_b is the Brinell hardness of the drill bit material and A_{ch} is the indentation area associated with the chisel edge, and computed from the chisel edge angle ψ_c as in [29]:

$$A_{ch} = \frac{2wf}{\sin\left(\pi - \psi_c\right)\cos\kappa_t}. \tag{12}$$

The total thrust force results:

$$F_{th} = F_{th,ch} + 2\int_0^R \mathrm{d}F_{th,lip} \approx F_{th,ch} + 2\sum_{j=1}^{n_e}\Delta F_{th,j}. \tag{13}$$

Moreover, the total cutting torque is computed as:

$$C_t = 2\int_0^R r\mathrm{d}\overline{F}_c \approx 2\sum_{j=1}^{n_e} r_j\Delta F_{c,j}. \tag{14}$$

Hence, the total drilling power is defined as the sum of the thrust and cutting powers:

$$P_d = P_c + P_{th} = C_t\omega + F_{th}V_f, \tag{15}$$

where ω is the angular velocity of the drill bit and $V_f = 2\pi\omega c$ is the feed speed.

At last, it is possible to define the thermal energy dissipated during drilling. A partition coefficient β is defined to determine the portion of heat flowing either into the workpiece or in the chip-tool pair:

$$P_d = \left(P_{d,chip} + P_{d,tool}\right) + P_{d,wp} = \beta P_d + (1-\beta)P_d. \tag{16}$$

The definition of the partition coefficient β is challenging, and it is normally correlated to the cutting parameters. Segurajauregui et al. [24] derived this parameter by matching experimental temperature values with FEM simulation. They found that it ranged between 6 and 53% and decreased both with the cutting velocity and the feed rate. Another approach was carried out by [23], where the heat exchanged with the workpiece is computed as the sum of the energy generated on the shear plane and the contact between the flank face of the tool and the finished workpiece surface. The approach employed in this work is based on an analysis of the experimental campaign conducted by [24]. In that study, twenty drilling tests on aluminium were performed, considering five cutting velocities (ranging from 50 to 300 m/min) and four feed rates (from 0.15 to 0.5 mm/rev). Based on the experimentally derived partition coefficients, a logarithmic correlation was developed in the present work to relate the partition coefficient to both feed rate and cutting velocity. The resulting logarithmic fit accurately reproduces the experimental data, achieving an R2 value of 0.987:

$$\beta = K_0\cdot\ln(V) + K_1\cdot\ln(c) + K_2 = -0.202\cdot\ln(V) - 0.175\cdot\ln(c) + 1.003. \tag{17}$$

The fitting is presented in Fig. 4

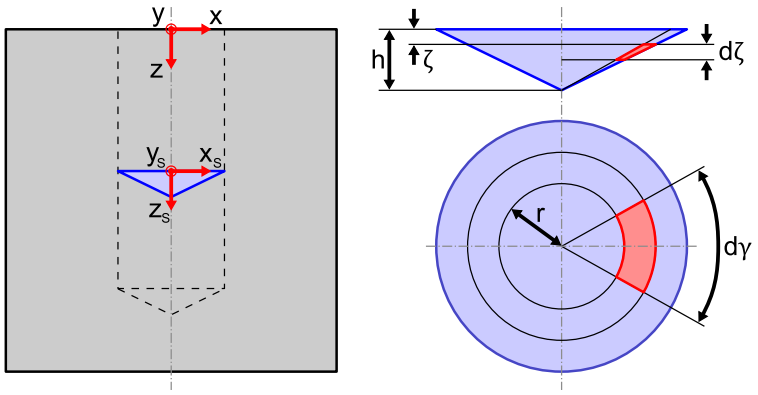

Fig. 5. (left) Fixed and moving coordinate system for temperature field computation. In blue, the conical heat source surface. (right) Details for thermal field solution integration over the drill bit surface.

2.1.2. Analytical thermal model

The analytical thermal model conceived for peck drilling was formulated leveraging the work by Shi et al. [30]. The drilling operation here is approximated as a moving non-dimensional heat source that conducts heat in a solid domain. The heat equation for a stationary point source is the following [46]:

$$T(x,y,z,t) = \frac{Q}{(4\pi\alpha t)^{3/2}} \exp\left[-\frac{(x-x_s)^2+(y-y_s)^2+(z-z_s)^2}{4\alpha t}\right], \tag{18}$$

where x_s, y_s and z_s are the point source coordinates, α is the thermal diffusivity and Q is the source heat expressed as $\frac{E_{th}}{\rho c_p}[Km^3]$, where E_{th} is the released thermal energy released instantaneously at $t = 0$, ρ is the material density and c_p the specific heat capacity. $T(x,y,z,t)$ is the temperature field generated by the point source in the infinite solid medium (i.e., the workpiece).

For peck drilling, the solution has to be generalised, since the heat source is not stationary but is moving inside the workpiece. So, the axial position coordinate z_s has to be described as a function of the generic release time t_s:

$$z_s = f(t_s) = z_p(t_s) + z_0, \tag{19}$$

where z_0 is the initial source position and z_p is the generic source displacement at time t_s.

Moreover, the heat source must continuously (or intermittently) release heat inside the workpiece. This is accounted through the superposition principle, thus integrating Eq. (18) with respect to time, and including in the formulation Eq. (19). Therefore, the temperature field equation becomes:

$$T(x,y,z,t) = \int_0^t \frac{q(t_s)}{\rho c_p \left(4\pi\alpha(t-t_s)\right)^{3/2}} \exp\left[-\frac{(x-x_s)^2+(y-y_s)^2+(z-z_s(t_s))^2}{4\alpha(t-t_s)}\right] \mathrm{d}t_s, \tag{20}$$

where $q(t_s)$ is the thermal power released by the point source at time instant t_s, and we assume that the power is generated from time instant 0 to t. Since the thermal power during cut is generated on the drill bit surface (which can be considered conical over a drill bit revolution), the solution must be generalised on a 2D surface.

The solution in Eq. (20) is considered to be released on an infinitesimal conical element at a generic radius r from the drill bit centre. With reference to Fig. 5, the infinitesimal conical element has area $\mathrm{d}A$ computed as:

$$\mathrm{d}A = \frac{r\mathrm{d}\gamma\mathrm{d}\zeta}{\cos(\kappa_t)}, \tag{21}$$

where ζ is the axial position of the infinitesimal conical element from the drill bit reference system coordinate z_s. γ is the circumferential position of the infinitesimal conical element from x_s.

Indeed, the final solution in an infinite medium is obtained by integrating (Eq. (20)) over the conical surface of the drill bit:

$$T(x,y,z,t) = \int_0^t \int_0^h \int_0^{2\pi} \frac{q(t_s)r}{\rho c_p S\cos(\kappa_t)(4\pi\alpha(t-t_s))^{3/2}} \exp\left[-\frac{(x-x_s)^2+(y-y_s)^2+(z-z_s(t_s)-\zeta)^2}{4\alpha(t-t_s)}\right] \mathrm{d}\gamma\mathrm{d}\zeta\mathrm{d}t_s, \tag{22}$$

where $r = (h-\zeta)\tan(\kappa_t)$; $x_s = r\cos(\gamma)$ and $y_s = r\sin(\gamma)$; $S = \pi Ra$ is the lateral area of cone and a is the cone apothem. Eq. (22) refers to the temperature field generated by the drill bit cone centre in $(x_s, y_s, z_s(t_s))$, releasing heat from time $t_s = 0$ to time $t_s = t$, in an infinite workpiece. This means that $q(t_s)$ can be computed as the fraction of power introduced into the workpiece $q(t_s) = (1-\beta)P_d(t_s)$. The introduced heat is modelled as a flux computed by dividing the cutting power by the cone area S, thus representing the average heat exchanged between the drill and the workpiece over a complete revolution. By imposing this average heat transfer, temperature fluctuations near the drill cannot be captured; however, due to the thermal inertia of the material, these fluctuations are highly localised near the cutting edge and have a negligible effect on the overall temperature field. As a result, this approach provides an accurate representation of the workpiece temperature. A similar modelling strategy has been previously employed for drilling thermal analyses (Patne et al. [23]).

Semi-infinite medium. Eq. (22) is valid in the hypothesis of an infinite solid workpiece. That is not true for the analysed case and in general when the volume of the workpiece is not negligible (see Section 2.2). Since the holes of Section 2.2.2 are performed close to the edges of the workpiece to facilitate temperature measurements, boundary conditions must be introduced at workpiece surfaces. To do so, mirrored virtual heat sources are be placed in the system. This approach allows to introduce adiabatic and isothermal boundaries in the problem. Virtual mirroring is performed with respect to the boundary surface to be introduced in the model. In Fig. 6, an illustration of the application of adiabatic and isothermal boundary conditions is shown, as well as the combinations of heat sources required to achieve these conditions. When an isothermal boundary surface must be introduced, the virtual heat source is introduced with negative power. Indeed, this source becomes a heat sink because the net flux moves from the real heat source to the virtual heat source. Since the real heat source produces a temperature field on the boundary surface equal in magnitude but of opposite sign with respect to the field generated by the heat sink, the net temperature increase on the boundary surface is null. When an adiabatic boundary surface is instead considered, a positive power virtual surface must be introduced. In this way, the two fluxes across the mirroring surface are equal and opposite, generating a different temperature field. In the analysed case (Section 2.2), the workpiece is considered limited in two directions and infinite along the remaining

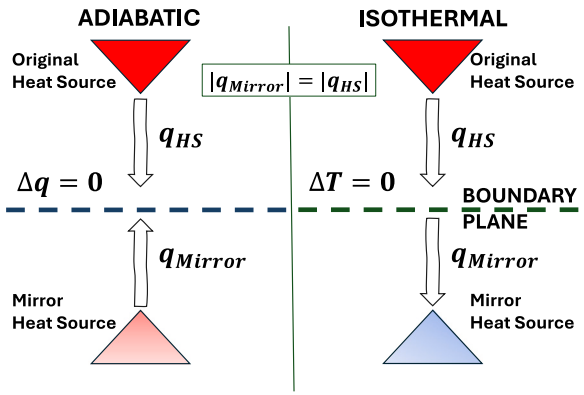

Fig. 6. Mirror source boundary condition approach. Adiabatic and isothermal schemes.

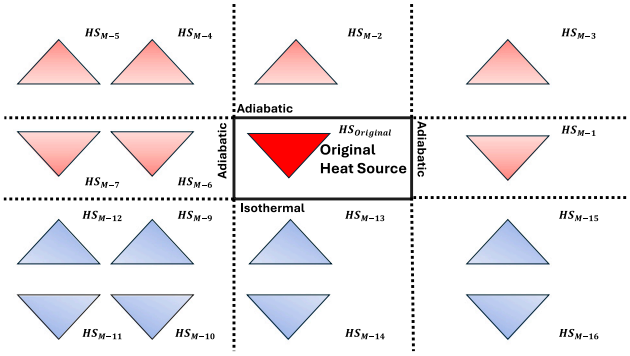

Fig. 7. Mirroring heat source scheme of the analysed case. The real source term is located in the centre. Blue sources are heat sinks, red are positive sources.

axis. The workpiece upper surface is considered adiabatic, as well as the two lateral surfaces (no heat exchange towards air is considered). The bottom surface is considered isothermal because it is in contact with the dynamometric table and consequently with the pallet (considered with infinite thermal inertia). Referring to Fig. 7, HS-original thus represents the real heat source, whereas others are all virtual and mirrored heat sources.

The temperature field in the finite medium is obtained by superposition of the temperature field of each source j (real and virtual):

$$T_{sf}(x, y, z, t) = \sum_{j}^{n_s} T_j(x, y, z, t), \tag{23}$$

where n_s is the total number of real and virtual sources.

2.1.3. Finite volume thermal model

The finite volume approach is a method for representing and evaluating partial differential equations (PDE) in the form of algebraic equations. It uses a volume integral formulation of the problem with a finite partitioning set of volumes to discretise the equations. It is the methodology most used in Computational Fluid Dynamics, however, it is suitable for every physical problem that is based on the definition of a set of transport equations, as the heat transfer problem in analysis. In the specific case, the physical quantity that must be transported in the domain is the energy, and in particular, the enthalpy h. This transport equation is written as follows:

$$\frac{\partial \rho h}{\partial t} - \Delta(\alpha \cdot h) - \nabla \cdot (\rho h \phi_{mesh}) = S_h, \tag{24}$$

where α is the thermal diffusivity, ρ the density, ϕ_{mesh} is the mesh flux on finite volume faces, defined as the scalar product between the face

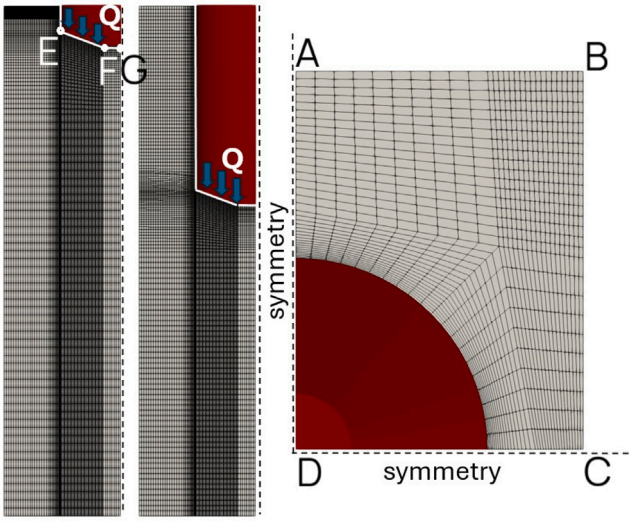

Fig. 8. FV numerical domain. Two time instants are represented to highlight grid motion. The patch of application of thermal power is highlighted by arrows.

velocity and its normal vector, and S_h is a general source term. The third term of the equation, referred to as the mesh flux correction, accounts for the heat flux associated with the removal of material due to mesh motion. It is defined as the product of the density, the energy, and the mesh flux, the latter representing the surface flux component induced by mesh deformation. This correction compensates for the mesh motion to prevent non-physical heat fluxes from appearing within the workpiece.

The first step of the simulation pre-processing is the definition of the numerical domain. As shown in Fig. 8, which represents the mesh with the boundary conditions at different steps of the drilling process, symmetric geometrical characteristics are exploited to reduce the computational cost of the analysis: only one quarter of the drilled hole is modelled, and symmetric boundary conditions are applied along the planes of geometrical symmetry (planes AD and DC). In the present physical problem, these symmetry conditions correspond to a null normal enthalpy gradient. An adiabatic boundary condition is applied to the plane where the experimental domain is truncated (plane AB), this is justified because the surface is sufficiently distant from the thermocouple location. No tool-drilling hole wall friction and/or heat transfer model has been adopted in this work; hence, an adiabatic boundary condition is applied in correspondence with the drilling hole walls. In addition, a convective boundary condition is imposed on the faces representing the end of the workpiece (plane BC). The thermocouple is positioned on plane DC. The starting mesh is purely hexahedral, and it is set to have a refined and homogeneous cell size in correspondence to the drilling wall to have a correct simulation of the temperature field and thus a reasonable comparison with the experimental measurement. To account for material removal, the mesh is deformed according to the imposed cutting profile, an example of which is shown in Fig. 1. The deformation is implemented by prescribing a displacement to the boundary faces corresponding to the drill bit head (edges EFG in Fig. 8). As a consequence, the surrounding mesh adapts to accommodate the resulting geometric variation. The deformation is computed using the *displacementComponentLaplacian* algorithm, which determines the mesh point displacements by solving the cell-centre Laplacian for the prescribed motion direction. Since the mesh is only deformed and there are no topological changes (addition or removal of mesh layers), the number of cells remains constant during the simulation.

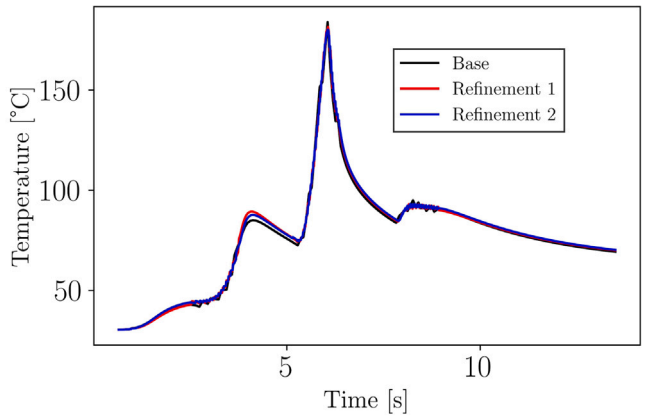

Fig. 9. Mesh sensitivity analysis result on operating condition ID. 1. Temperature sampled on thermocouple location.

Table 1
Mesh sensitivity analysis statistics.

Mesh	Coarse	Refinement 1	Refinement 2
n. cells	29 870	170 000	806 490
Min. cell Volume mm^3	1.05e−3	6.45e−3	1.32477e−5
Max. cell Volume mm^3	4.84e−1	5.9e−2	1.83e−2
Max. cell Volume mm^3	7.19e−2	8.9e−3	2.63e−3
Max non-orthogonality	7.54	7.65	7.68

Regarding the discretisation schemes, an Euler scheme is applied for the time derivative, while linear discretisation schemes are used for the divergence and Laplacian terms. The heat released by the cutting process, obtained from the mechanical cutting model, is applied to the lip boundary patch (patch EF) as a time-dependent imposed heat flux boundary condition. The applied heat flux is active and computed from Eq. (16) during the drilling phase, while it is set to zero when the drill bit retracts and returns to the workpiece surface.

The final mesh size was selected based on a mesh sensitivity analysis. Specifically, three meshes containing 29870, 238960, and 806490 cells were tested under one operating condition. The meshes were generated by uniformly scaling the number of cells in all three spatial dimensions, and their statistics are summarised in Table 1. The simulations were performed for operating condition ID 1 (conditions presented in Table 3), and the analysis was based on the temperature evolution at the thermocouple location. As visible in Fig. 9, the three meshes produced comparable results, particularly for the two finer grids. Therefore, the mesh with the first level of refinement was selected for the subsequent analyses, as further refinement did not significantly improve the accuracy but led to a substantial increase in computational cost.

2.2. Experimental setup

Experiments consisted of a set of drilling tests performed using a Mandelli M5 machine tool. The 4-axis machine tool has a horizontal spindle with a maximum speed of 7000 rpm, a maximum torque of 120 Nm, and a maximum power of 65 kW. Each hole was machined following a peck drilling strategy characterised by 5 pecks, in dry conditions. The position and speed of the drill bit for the peck drilling strategy are represented in Fig. 10 (top). The drill bit is first placed at 100 mm from the workpiece. The cycle starts with rapid speed reaching 40 mm from the workpiece. The drill bit approaches in rapid the dwell position at 4 mm from the surface. Here, the peck 0 (performed in air) is done at a lower feed rate compared to the nominal experiment feed, and it has the purpose of creating the centring mark. The remaining 4 pecks (identified Fig. 10 through enclosed numbers), the focus of our analysis, are 3 mm deep, for a total depth of the hole of 12 mm. After each peck, the drill bit stands still within the hole for 0.7 s, then exits the hole to evacuate the chip, returning at 4 mm far from the surface. After the last peck, the tool exits directly in rapid mode at the safety position of 40 mm from the surface and then at 100 mm.

Table 2
Twist drill parameters.

Parameter	Symbol	Value
Cutting edge diameter	$2R$	8.8 mm
Cutting edge length	L_c	35 mm
Overall length	l_1	89 mm
Projection length	l_2	47 mm
Shank diameter (h6)	d_1	10 mm
Taper angle	$2\kappa_t$	140°

10 holes were machined on the surface of the AISI316L workpiece, which was shown in Fig. 11 and whose properties are reported in Section 2.2.3. The workpiece exposes a surface where up to 18 holes can be drilled (Fig. 11(b)). Each hole is positioned at 6.7 mm from the side and has a diameter $2R = 8.8$ mm, corresponding to the drill bit diameter. The distance between two subsequent holes is 13.1 mm. On the side of the workpiece, micro-holes were pre-drilled in correspondence with the holes' axes. Micro-holes were drilled 8.3 mm far from the surface of the workpiece. Such micro-holes were used as positioning slots for a thermocouple, with the aid of a support comb (see Fig. 11(c)). With a depth of 2.1 mm, micro-holes allowed to position a thermocouple at 0.2 mm from the experimentation hole, in the middle of the third peck (Fig. 11(b)). Positioning the thermocouple so close to the drilling hole allows sampling of temperatures representative of the maximum temperature reached inside the domain, a parameter that directly affects machining quality indicators such as hole distortion. The location of the thermocouple with respect to the signals is also shown in Fig. 10.

A particular tool holder offered by Gühring was employed to reduce the impact of tool run-out. Two solid carbide drills A3293TTP-8.8 with AlTiN coating, provided by Walter, were used for the experimental tests, whose characteristics are listed in Table 2. In order to apply the method, the rake angle of the drill bit should be computed along the radial coordinate. To do so, it is possible to apply the method for general twist drill bits provided in the work of Minunkhin et al. [28]. Nevertheless, Walter drill bits featured a ground chisel surface. Experimental identification of the rake angle at the centre and at the outer part of the lip was carried out through a Keyence VHX7000 digital microscope. The results of the identification were used to tune the initial and final value of the drill bit rake angle, while the trend along the radial coordinate was determined through the use of the general twist drill method in [28]. The resulting drill bit rake angle profile and consequently the inclination and reference angles are shown in Fig. 12.

2.2.1. Data acquisition system

The data acquisition system is composed of a NI cDAQ9174, capable of acquiring different quantities associated with the drilling process. The data acquisition system was connected to a *DELL* laptop equipped with *Labview*.

As shown in Fig. 11(a) a Kistler 9265 A dynamometric plate was placed underneath the workpiece, to measure the thrust cutting force generated by the drill bit on the workpiece. The measurement of drilling temperature was carried out by means of a workpiece-embedded thermocouple Tersid MTS-15000 Series Type K ϕ 0.5 mm with isolated junction, covered with an Inconel-made sheath and insulation with magnesium oxides. The positioning of the thermocouple was aided by the use of the support comb shown in Fig. 11(a) and 11(c). A spring included between the comb and the thermocouple guaranteed repeatable positioning of the thermocouple within the micro-hole. Electrical spindle power P_s was acquired through a power meter. The adopted

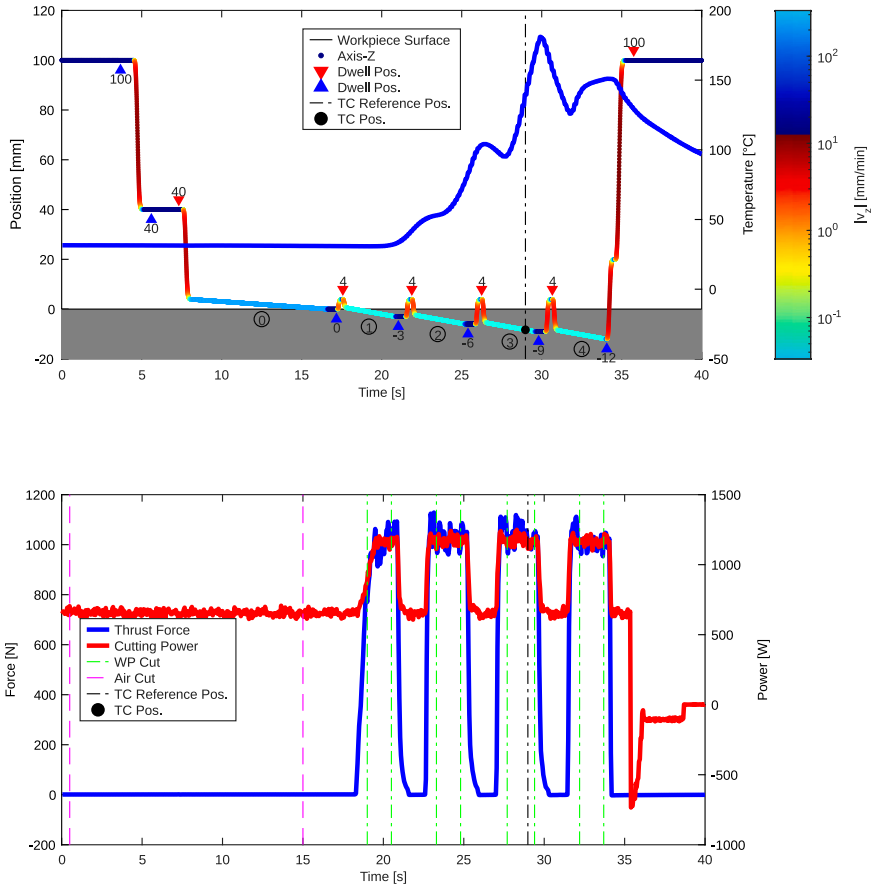

Fig. 10. Peck drilling strategy: (top) position of the axis is shown on the left axis (colour represents the absolute value of z-axis speed); blue line shows the workpiece temperature at the thermocouple location and is plot on right axis; enclosed numbers identify the pecks; black circle shows the position of the thermocouple, and dash-dot black line shows the time at which the drill bit reached the depth of the thermocouple; (bottom) thrust force, measured from the dynamometer is shown on the left axis; spindle power is shown on the right axis; magenta dashed lines shows region for air cutting measurement; green dash-dotted lines show regions for peck cutting; dash-dot black line shows the time at which the drill bit reached the depth of the thermocouple.

sampling frequency was $f_s = 20$ kHz. This frequency was necessary to minimise the aliasing effect due to the electrical measurements carried out on the electrospindle. In fact, the electrospindle is controlled through Pulse Width Modulation (PWM). The voltage signal provided to the electrospindle (i.e., the first signal to be acquired) is therefore a square wave, including high-frequency harmonics. To measure it correctly, a high acquisition frequency allows for measuring the voltage signal spectrum.

The spindle active power $P_s(t)$ was calculated in real-time as:

$$P_s(t) = i_1(t)v_1(t) + i_2(t)v_2(t) + i_3(t)v_3(t) \tag{25}$$

The three-phases voltages (v_1, v_2, v_3) and the corresponding currents (i_1, i_2, i_3) were acquired through the properly designed power meter. Each current was measured using a sensor based on *Hall's* principle ($LEMLF205 - S/SP3$).

Signal filtering was applied to the high-frequency spindle power, and to the other quantities, i.e., thrust force $F_{th}(t)$ and workpiece temperature $T_{wp}(t)$, with a time interval $\Delta t = 0.05$ s. Indeed, the resulting acquisitions were acquired at a sampling frequency of 20 Hz. This is mainly needed to measure the effective power provided to the spindle (i.e., the one required by the process), and not the one instantaneous one (i.e., the one needed to control the electrospindle).

P_{sf} is the total spindle power drawn from the network. Thus, it is necessary to divide the total power into two contributions:

$$P_{sf}(t) = \frac{P_{air}(t) + P_d(t)}{\eta_s} \tag{26}$$

where $P_{air}(t)$ is the mechanical power required to run the spindle at the specified spindle speed, without cutting; η_s is the electrical efficiency of the spindle that considers the specific working condition of the spindle, see also Albertelli [47]. To derive the mechanical power $P_d(t)$ required by each peck of the drilling strategy, it was necessary to estimate P_{air}. For each drilled hole, as shown in Fig. 10 (bottom), P_{air} was estimated as the mean power in the safety region (identified by vertical dashed magenta lines) when the drill bit was far away from the workpiece. Cutting torque was also computed starting from the mechanical drilling power, as:

$$C_t(t) = \frac{60P_d(t)}{2\pi\omega} \tag{27}$$

where ω is the spindle speed in rad/s.

It was then possible to compute F_{th}^{exp}, C_t^{exp} and P_d^{exp} by averaging their values over each peck p (separated by dash-dotted green lines in Fig. 10 (bottom)), and then on the pecks:

$$\begin{aligned} F_{th}^{exp} &= \frac{1}{4}\sum_{p=1}^{4} \overline{F}_{th,p} \\ C_t^{exp} &= \frac{1}{4}\sum_{p=1}^{4} \overline{C}_{t,p} \\ P_d^{exp} &= \frac{1}{4}\sum_{p=1}^{4} \overline{P}_{d,p} \end{aligned} \tag{28}$$

Finally, real-time data associated to axis position and velocity of the linear axes and the spindle were acquired through the SinuCom

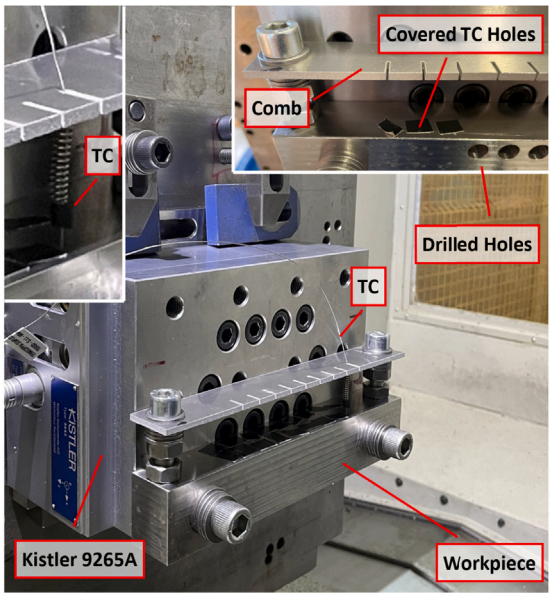

(a) Setup of the experiments, with details on thermocouple positioning.

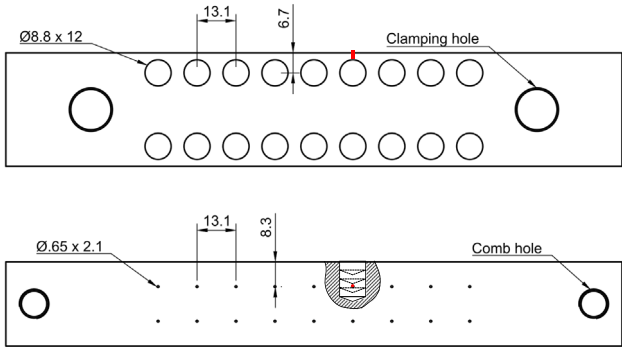

(b) Details of the workpiece, with grid of possible holes and thermocouple micro-holes. In red, the placement of the thermocouple for the sixth hole and the relative position with respect to the pecks.

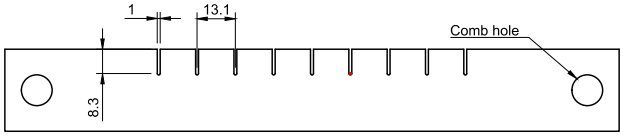

(c) Details of the comb supporting thermocouple positioning. In red, the placement of the thermocouple for the sixth hole.

Fig. 11. Conceived drilling experimental setup details.

NC acquisition system from Siemens. This system was used to access and store quantities from the numerical control of machine tools at a frequency of 250 Hz.

2.2.2. Experiments

In order to validate the proposed methodology, a set of experiments was designed. The objective was to assess the prediction capabilities of the conceived numerical model under different combinations of feed rate per revolution (c) and cutting velocities (V). A set of 10 holes was performed on the workpiece described in Section 2.2. The experiments were generated with a full-factorial design (2^k+1). k stands for the number of parameters varied in the design, i.e., c and V. Each parameter is tested on 2 levels. Moreover, a central point was added with average feed c and cutting speed V values. All the tests were replicated twice, and the replicates were carried out on two identical drill bits. Randomisation was performed to minimise the impact of confounding variables, such as the border effect. The sequence (and location in the workpiece) of the 10 holes was randomised to minimise the border-effect influence on the measured physical quantities. The resulting DoE campaign was shown in Table 3 (odds test IDs are made with the first drill bit, evens with the second):

Explanatory trends of measured workpiece temperature were shown in Fig. 10(top), while trends for thrust force and acquired power were shown in Fig. 10(bottom). The values of the experimental thrust force and cutting power characterising the drilling process were computed as the mean of the values related to the four cutting phases of the tool.

2.2.3. Framework generalisation and material characterisation

The modelling framework proposed in this work is applicable to any drilling configuration. The predictive machining model utilises the

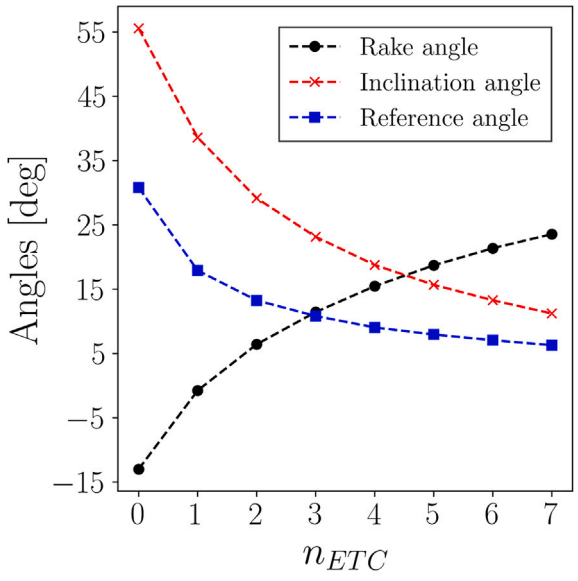

Fig. 12. Rake, inclination and reference angles evolution along the drill lip, used in the oblique cutting model. Lip (x-axis) is discretised in ECTs.

Johnson–Cook flow stress model to characterise the material's constitutive behaviour during machining and incorporates drill bit geometric

Table 3
Experimental tests parameters according to the DoE. c is the feed per revolution, V the cutting speed, S the spindle speed, F the thrust force. Odds test IDs are made with the first drill bit, evens with the second.

Test ID	c [mm/rev]	V [m/min]	n [rpm]	V_f [mm/min]	F_{th}^{exp} [N]	$\overline{F_{th}^{exp}}$ [N]	$CV_{F_{th}^{exp}}$ [%]	P_d^{exp} [W]	$\overline{P_d^{exp}}$ [W]	$CV_{P_d^{exp}}$ [%]
1	0.048	40	1447	69	1026	1073	6.19	510	515	1.37
2	0.048	40	1447	69	1120			520		
3	0.112	40	1447	162	1720	1945	16.36	1106	1075	4.01
4	0.112	40	1447	162	2170			1045		
5	0.048	60	2170	104	1190	1080	14.40	610	691	16.57
6	0.048	60	2170	104	970			772		
7	0.112	60	2170	243	1800	1750	4.04	1238	1250	1.36
8	0.112	60	2170	243	1700			1262		
9	0.080	50	1809	145	1590	1685	7.97	902	915	2.01
10	0.080	50	1809	145	1780			928		

Table 4
Material characterisation.

Johnson Cook parameters for AISI 316L [48]		
A	412	$[MPa]$
B	761	$[MPa]$
C	0.038	–
n	0.510	–
m	0.520	–
Thermal Conductivity [49]		
k	$9.2848 + 0.0157 \cdot T[K]$	$\left[\frac{W}{mK}\right]$
Heat Capacity Coefficient [49]		
c_p	$459.32 + 0.1328 \cdot T[K]$	$\left[\frac{J}{kgK}\right]$

cutting angles. Both thermal models require drill bit and workpiece geometry as input parameters, while workpiece material thermo-physical properties are employed throughout all models. Once these parameters are identified for a specific drilling operation, users can input them into dedicated dictionaries, thereby enabling broad application of the methodology across different scenarios. For substantially different drilling configurations, recalibration of the partition coefficient (Eq. (16)) may be necessary, as this parameter depends on cutting-edge design and chip evacuation characteristics. For the methodology validation presented in this study, the Johnson–Cook model parameters for AISI 316L proposed by Amor [48] were employed, and the thermal conductivity and heat capacity coefficients were treated as temperature-dependent linear functions using coefficients proposed by Kim [49]. Table 4 provides a summary of the material characterisation, while Section 2.2 and Table 2 describe the drill bit in analysis.

3. Results and discussion

The developed methodology was applied to the cases represented in Table 3. The mechanistic model results are first analysed, followed by the validation of the cutting temperature with both the analytic and FV models.

3.1. Mechanical analysis

The results of the mechanical model in terms of thrust force and power are presented in Table 5. Since two different drilling holes were performed under the same conditions, the model results are compared with the experimental average $\overline{\phi_{exp}}$. To define the accuracy of the results, a relative error has been defined for each quantity (ϕ) as:

$$err_\phi[\%] = \frac{\phi_{mod} - \overline{\phi_{exp}}}{\overline{\phi_{exp}}} \cdot 100. \tag{29}$$

The average of the errors is 4.66% for the power and 7.45% for the thrust forces. The least accurate results are achieved in the tests

Table 5
Mechanical model results.

Test ID	$F_{th,lip}$ [N]	F_{th} [N]	$err_{F_{th}}$ [%]	P_{cut} [W]	P_d [W]	err_{P_d} [%]
1,2	944	1028	4.38	491.30	493	4.46
3,4	2069	2265	14.13	1080.96	1087	1.10
5,6	854	938	15.13	678.35	680	1.62
7,8	1602	1798	2.67	1349.08	1353	7.62
9,10	1529	1669	0.96	995.75	1000	8.50

characterised by the highest Coefficient of Variation (CV), defined as the ratio between the standard deviation (σ_ϕ) and the average value of the specific quantity:

$$CV_\phi[\%] = \frac{\sigma_\phi}{\overline{\phi}} \cdot 100. \tag{30}$$

Such variations can be explained by differences in cutting edge geometry, which arise from machining tolerances and result in slightly different cutting angles between the tools. Since the lip cuts the majority of the chip and the feed velocity is much smaller than the rotating one, the contribution of the feed power to the overall mechanical one is small (Eq. (16)). Indeed, the cutting power is very close to the total power.

3.2. Thermal analysis

Fig. 10 shows an experimentally measured temperature profile alongside the corresponding drill penetration, to clarify the evolution of temperature during the process. The four pecking steps are clearly distinguishable in the temperature evolution and are slightly delayed from the drilling profile due to the thermal inertia of the workpiece. The highest temperature occurs during the third peck, as the tool is closest to the measurement location, reducing the distance for heat to diffuse through the material.

In the final peck, a significant temperature increase is measured, even though the drill bit has passed below the measurement point. This trend occurs even if the cutting region moves away from the measuring point due to the friction between the chip and the hole side wall during its evacuation, as well as heat conduction with the tool. Specifically, during the chip motion inside the drill bit, the chip is pressed against the drill wall by centrifugal force, generating friction that dissipates heat into the workpiece. Additionally, the drill bit becomes increasingly hot during operation and transfers heat to the hole wall.

This phenomenon is well-documented in deep drilling and leads to the development of a depth-dependent force component known as the evacuation force [50,51]. However, the current drilling condition is not classified as deep drilling, since the depth is only 1.4 times the drill diameter. Consequently, no significant increase in cutting power with depth is observed. Still, the portion of this power that is dissipated thermally into the workpiece is captured by the measurement, as the thermocouple is located just 0.2 mm from the hole surface.

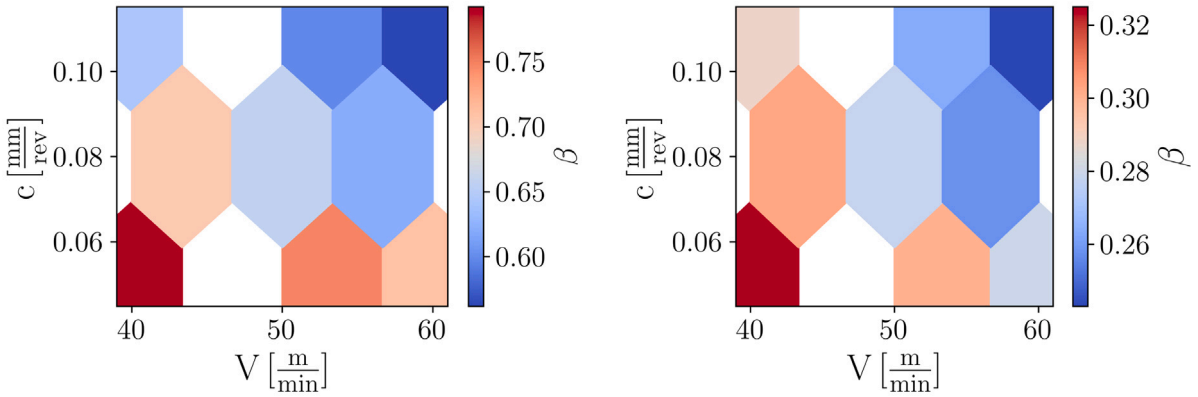

(a) Estimated partition coefficient for analysed case based on experimental fitting based on database in [24]

(b) Estimated partition coefficient for analysed case based on new fitting coefficients

Fig. 13. Sensitivity analysis on power partition coefficient.

The partition coefficient β used in the analysis was derived from Eq. (17); however, it required calibration to fit the specific tools, cutting conditions and workpiece material, which differed from those in the original reference. To achieve this, three test IDs—1, 5, and 9 were used to fit Eq. (17). The fitted coefficients were: $K_1 = -0.111$, $K_2 = -0.044$, and $K_3 = 0.602$. These values were applied to the remaining tests. Fig. 13 shows a sensitivity analysis comparing the original database fitting [24] (Fig. 13(a)) with the tuned fitting used here (Fig. 13(b)). The new fitting leads to a smaller partition coefficient, which can be attributed to the different material drilled. The literature analysis was performed on aluminium, while this work examines stainless steel. Aluminium has a thermal diffusivity approximately four times greater than stainless steel (97 mm^2/s vs. 20 mm^2/s). Consequently, at constant mechanical power, heat generated in aluminium diffuses more easily throughout the material. In contrast, heat in steel remains more localised near the chip, resulting in a larger portion of total heat being dispersed by the chip. Both fittings follow the same trend with varying cutting velocity and feed rate, since these parameters affect heat diffusion independently of the workpiece material. Specifically, faster cutting reduces the time available for heat to diffuse into the workpiece, increasing the heat stored in the chip. The resulting partition coefficients for the specific test conditions are summarised in Table 6, these values align with Fleischer et al.'s literature review on dry drilling [25], which reports a range from 0.1 to 0.35.

The temperature profiles of the two thermal models and the experimental measurements are compared in Fig. 15. For each set of operating parameters, the error function is also represented for both modelling strategies (Eq. (29)), calculated with respect to the average between the two drill bit measurements. Given the same operating conditions, the tests performed using the second drill bit show a higher temperature than those conducted with the first one. This difference is attributed to the higher mechanical power demand of the second drill bit, highlighting the variability inherent in drilling (Section 3.1), even if the nominal conditions are identical.

By comparing the numerical simulations with the experimental temperature curves, the drilling operation can be divided into two phases based on the relative position of the thermocouple and the drill bit, as illustrated in Fig. 14. In the first phase, when the drill bit is above the thermocouple, the sensor is embedded within the uncut workpiece material. Temperature increases in this stage are primarily due to heat conduction from the cutting zone through the material. In the second phase, after the drill bit has passed the thermocouple, the sensor is located near the inner surface of the hole. At this point, secondary heat sources, such as friction and heat exchange between the chip and the drill bit, are captured by the measurement system.

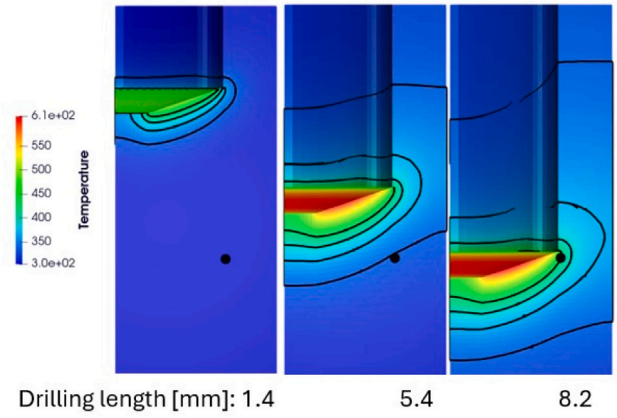

Fig. 14. FVM Simulated temperature profile at different time steps, thermocouple location highlighted by black point.

In the first phase of drilling, for all simulated cases and both models, the calculated temperature profiles well represent the average experimental measurement. The average error in this region is well below 10% for all the cases, and it is computed as follows:

$$\overline{err_{T_{max,FVM}}}\,\% = \frac{1}{t(T_{Max})} \cdot \int_0^{t(T_{Max})} |err_T\,\%|\,dt. \tag{31}$$

This indicates that both the primary heat source, plastic energy dissipation, and the heat conduction within the material are being accurately modelled. In the second phase, the models tend to under-estimate the temperature, since the secondary heat sources described above are not modelled. A similar trend was reported by Patne [23] in an analysis of drilling in titanium alloys. In that study, the model overestimated the temperature at a measurement point located 1 mm from the drilling hole, five times farther from the hole than in the present work. The discrepancy was observed only for the thermocouple closest to the hole and diminished with increasing distance. This observation supports the interpretation that the temperature rise measured in our experiments is particularly pronounced because the thermocouple is positioned very close to the hole wall (0.2 mm). Test case 6 (Fig. 15(b)) represents the most critical condition due to the significantly higher mechanical power required by the second drill bit under these specific parameters.

Comparing the predictions of the two models, the largest discrepancies emerge after the drilling head passes the measurement location.

Table 6
Maximum temperature for computed and measured data.

Test ID	β [-]	T^{An}_{sample} [°C]	T^{FVM}_{sample} [°C]	$\overline{T^{exp}_{sample}}$ [°C]	$CV_{T^{exp}_{sample}}$ [%]	$err_{T_{max,Analytic}}$ [%]	$err_{T_{max,FVM}}$ [%]	$\overline{err_{T_{max,An}}}$ [%]	$\overline{err_{T_{max,FVM}}}$ [%]
1,2	0.325	155.81	173.5	188	3.70	17.13	7.72	5.84	3.54
3,4	0.288	177.71	181.53	181.3	2.48	1.98	0.11	4.13	6.41
5,6	0.280	157.82	161.25	178.17	15.01	11.41	9.49	4.44	6.30
7,8	0.243	150.81	135.82	132.78	5.11	13.58	10.4	6.51	8.44
9,10	0.278	179.10	176.34	156.95	3.04	14.11	12.3	7.33	4.64

These differences stem from the distinct model formulations. The analytical model treats the heat source as a moving bi-dimensional cone, without accounting for material removal. As a result, it allows heat to propagate both downward (towards positive z in Fig. 5) and upward (towards negative z in Fig. 5) within the workpiece. In contrast, the FVM simulation includes the geometrical effect of the material removal, which restricts heat conduction primarily to the region below the cutting plane and only partially towards the side of the hole. Therefore, once the drill bit moves past the thermocouple position, the FVM heat source continues propagating downward only. In contrast, the analytical model allows some heat to conduct upward, towards where the drill bit should be located and back towards the thermocouple. This difference causes the temperature to decrease more rapidly in the FVM simulation compared to the analytical model. Notably, the experimental temperature curve aligns more closely with the analytical results, suggesting that thermal interaction between the drill bit and the hole wall, neglected in the FVM model, plays a significant role. The analytical model implicitly accounts for this effect through its symmetrical heat propagation assumption.

To more accurately represent the thermal influence of the tool in the FVM simulation, a coupled model could be implemented. This would involve a separate thermal simulation of the drill bit and the application of a heat transfer boundary condition on the interface between the tool and the workpiece.

A quantitative comparison between simulated and experimental data is performed at the point of maximum temperature, hence, when the cutting edge passes the measurement location. This point is chosen because it is a key indicator of tool wear and potential dimensional inaccuracies. As shown in Table 6, the average error in predicting the temperature peak is 8% for the FVM and 11.64% for the analytical model.

No clear correlation is observed between the temperature peak and most operational parameters, except for cutting velocity. The peak temperature tends to decrease with increasing cutting velocity, a trend that mirrors the behaviour of the partition coefficient β.

This relationship can be attributed to the thermal inertia of the workpiece. At lower cutting velocities, the feed velocity (V_f) is also reduced, leading to a longer exposure time of the thermocouple to the heat source. Importantly, no direct correlation is found between cutting power and the maximum temperature in the workpiece. While cutting power increases with both feed rate and cutting velocity, the partition coefficient evolves in the opposite direction. This creates a balancing effect: as power increases, a greater portion of heat is dissipated through the chip and the drill bit, while a smaller portion accumulates in the workpiece.

3.3. Computational cost

The computational costs of the proposed models are as follows: 600 s/processor for the mechanical machining model, 60 s for the analytical thermal model, and 3000 s/processor for the FVM model. The mechanical model is relatively computationally expensive because the resolution of each ECT involves three nested loops, and no efficient optimisation algorithm has yet been implemented, since currently all possible parameter combinations are tested. There is therefore significant potential for improvement by introducing more efficient optimisation strategies; even simple methods such as the bisection algorithm could lead to substantial reductions in computational cost. Compared to FEM modelling of drilling, the FVM thermal model enables a significant reduction in computational cost, as it relies on an analytical model for the mechanics of cutting and therefore does not require direct resolution of the chip formation process, permitting the use of coarser mesh resolution and larger time steps. To provide a comparison of the computational cost associated with FEM simulations, Yıldız et al. [35] performed a finite element simulation of a drilling operation and estimated a simulation time of 15–20 days for the chip formation process, whereas Priest et al. [52] evaluated different FEM methodologies and software packages for drilling simulation, reporting simulation times ranging from 38 to 90 h. It should also be noted that the times reported above correspond to only a fraction of the drilling process, whereas the FVM model encompasses the entire peck drilling operation.

4. Conclusions

High cutting temperatures in drilling operations can significantly compromise both tool life and workpiece integrity. This temperature is affected by multiple factors, including tool and workpiece materials, cutting parameters, and the application of cutting fluids. Additionally, the chosen drilling strategy plays a crucial role in thermal management. This study introduces a predictive model specifically developed to evaluate the mechanical and thermal behaviour of peck drilling, a widely adopted technique aimed at mitigating excessive heat generation during drilling. The model strategy is based on the interaction of an analytical cutting model with two different thermal models for the temperature estimation. The following aspects have been treated:

- The mechanical model extends Oxley's machining theory to oblique cutting by incorporating the Johnson–Cook material model, enabling accurate predictions of cutting forces and power in peck drilling scenarios;
- The analytical thermal model captures transient heat conduction in a finite medium using a moving conical heat source representation;
- the FVM thermal model incorporates material removal via a dynamic mesh and solves the energy transport equations using OpenFOAM.

An experimental apparatus was conceived to validate both the thermal and the mechanical aspects of peck drilling. Experimental validation involved 10 drilling tests with varied cutting speeds and feed rates, using thermocouples embedded 0.2 mm from the hole surface. The model showed strong agreement with experimental data, in particular:

- Average error of 4.66% for cutting power prediction.
- Average error of 7.45% for thrust force estimation.
- Temperature prediction error of 8% for the FVM model and 11.64% for the analytical model.
- During the cutting phase (drill above thermocouple), both thermal models performed similarly with average temperature errors around 5.8%.

Discrepancies arose during the post-cutting phase due to the FVM model's neglect of tool–hole wall interaction, which the analytical

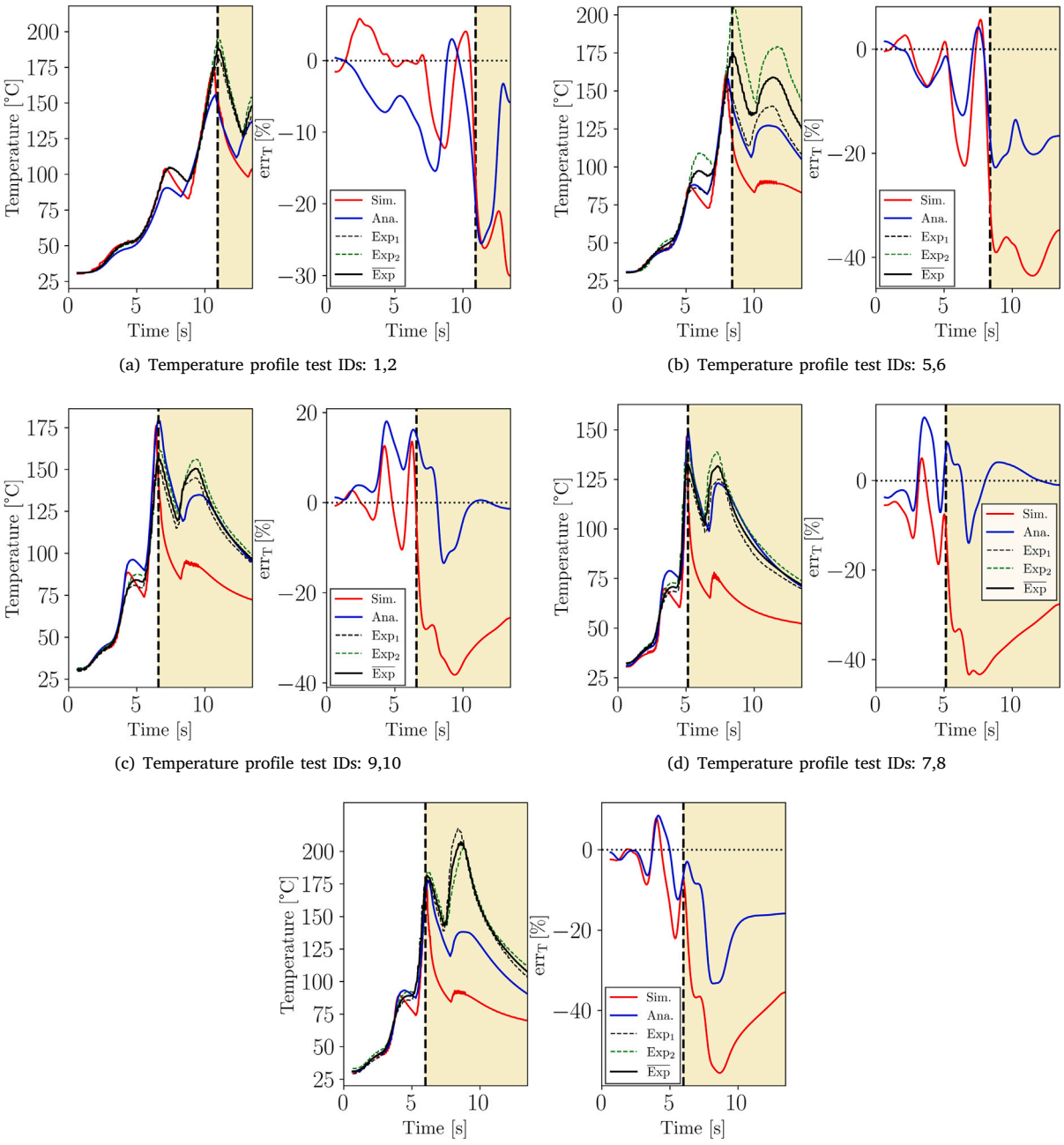

(a) Temperature profile test IDs: 1,2

(b) Temperature profile test IDs: 5,6

(c) Temperature profile test IDs: 9,10

(d) Temperature profile test IDs: 7,8

(e) Temperature profile test IDs: 3,4

Fig. 15. Left: Comparison of computed temperature curves for analytic (blue line) and FVM modelling (red line) with thermocouples measurements for test IDs: 1–9. The black line is the first drill bit, and the green line is the second. Right: error function for both models with respect to the average temperature measurement. Vertical line corresponds to thermocouple position. Fig. 10 can be used to correlate the temperature evolution to the peck position.

model captures more effectively through its symmetric heat propagation assumptions. Incorporating a frictional heat source could improve the accuracy of the model in this region. Future improvements on this topic could start from the definition of a time-dependent thermal input based on Han's chip evacuation force model [50]. This enhancement represents a valuable model refinement but requires dedicated experimental work beyond the current study's scope. The described model allows a prediction of both the mechanical and thermal aspects of peck drilling and hence can be useful as a design and/or diagnostic tool for a specific peck drilling condition. The analytical and FVM thermal models show comparable results for the specific analysis conducted. Therefore, for similar studies, the analytical model represents a computationally efficient approach for estimating the workpiece temperature during cutting. The FVM methodology, on the other hand, provides a powerful tool for performing more accurate and complex analyses. For instance, complex workpiece geometries, where no straightforward source-mirroring approach can be applied, can be simulated. Moreover, within the OpenFOAM framework, a direct coupling with the lubrication strategy can be implemented, similarly to what was previously proposed by the authors for cryogenic orthogonal machining [34]. The effect of thermally induced deformations could also be modelled in OpenFOAM, thanks to the availability of specific solvers for this purpose [53]. Hence, the present FVM model establishes the foundation

for more advanced analyses, which will be the focus of future works. Additional direction of research includes the possibility of modelling the amount of power flowing into the chip and into the tool, separately, aiming at modelling their temperature fields.

CRediT authorship contribution statement

Mattia Pelosin: Writing – review & editing, Writing – original draft, Visualization, Validation, Software, Methodology, Investigation, Formal analysis, Conceptualization. **Alessandro Moramarco:** Writing – review & editing, Writing – original draft, Visualization, Validation, Software, Methodology, Investigation, Formal analysis, Conceptualization. **Luca Bernini:** Writing – review & editing, Writing – original draft, Validation, Methodology, Conceptualization. **Paolo Albertelli:** Validation, Supervision, Methodology, Conceptualization. **Tommaso Lucchini:** Supervision, Methodology, Conceptualization.

Funding

This research did not receive any specific grant from funding agencies in the public, commercial, or not-for-profit sectors.

Declaration of competing interest

The authors declare that they have no known competing financial interests or personal relationships that could have appeared to influence the work reported in this paper.

References

[1] Ogedengbe T, Okediji A, Abioduna Abideen Y, Aderoba O, O.A. A, Alabi I, Alonge O. The effects of heat generation on cutting tool and machined workpiece. J Phys Conf Ser 2019;1378:1–10. http://dx.doi.org/10.1088/1742-6596/1378/2/022012.

[2] P P, Hiremath S. Mechanical peck drilling of inconel 625: Parametric analysis and grey fuzzy logic based multi-response optimization. J Micromanufacturing 2022;251659842211357. http://dx.doi.org/10.1177/25165984221135713.

[3] Zhao J, Ai X, Huang X. Relationship between the thermal shock behavior and the cutting performance of a functionally gradient ceramic tool. J Mater Process Technol 2002;129(1):161–6. http://dx.doi.org/10.1016/S0924-0136(02)00602-7, The 10th International Manufacturing Conference in China (IMCC 2002). URL: https://www.sciencedirect.com/science/article/pii/S0924013602006027.

[4] Seid Ahmed Y, DePaiva JM, Bose B, Veldhuis S. New observations on built-up edge structures for improving machining performance during the cutting of superduplex stainless steel. Tribol Int 2019. http://dx.doi.org/10.1016/j.triboint.2019.04.039.

[5] Bono M, Ni J. The effects of thermal distortions on the diameter and cylindricity of dry drilled holes. Int J Mach Tools Manuf 2001;41:2261–70. http://dx.doi.org/10.1016/S0890-6955(01)00047-5.

[6] Liao Z, la Monaca A, Murray J, Speidel A, Ushmaev D, Clare A, Axinte D, M'Saoubi R. Surface integrity in metal machining - part I: Fundamentals of surface characteristics and formation mechanisms. Int J Mach Tools Manuf 2021;103687. http://dx.doi.org/10.1016/j.ijmachtools.2020.103687.

[7] Soori M, Arezoo B. A Review in Machining-Induced Residual Stress. J New Technol Mater 2022;12(1):64–83, Publisher: Université Larbi Ben Mhidi de Oum El Bouaghi. URL: https://hal.science/hal-03679993.

[8] Abukhshim N, Mativenga P, Sheikh M. Heat generation and temperature prediction in metal cutting: A review and implications for high speed machining. Int J Mach Tools Manuf 2006;46(7):782–800. http://dx.doi.org/10.1016/j.ijmachtools.2005.07.024, URL: https://www.sciencedirect.com/science/article/pii/S089069550500180X.

[9] Kim DW, Lee YS, Park MS, Chu CN. Tool life improvement by peck drilling and thrust force monitoring during deep-micro-hole drilling of steel. Int J Mach Tools Manuf 2009;49(3):246–55. http://dx.doi.org/10.1016/j.ijmachtools.2008.11.005, URL: https://www.sciencedirect.com/science/article/pii/S0890695508002204.

[10] Pizzi M, De Gaetano F, Ferroni M, Boschetti F, Annoni M. A Deep-Hole Microdrilling Study of Pure Magnesium for Biomedical Applications. Micromachines 2023;14(1):132. http://dx.doi.org/10.3390/mi14010132, URL: https://www.mdpi.com/2072-666X/14/1/132.

[11] Eltaggaz A, Deiab I. Comparison of between direct and peck drilling for large aspect ratio in ti-6al-4V alloy. Int J Adv Manuf Technol 2019;102(9):2797–805. http://dx.doi.org/10.1007/s00170-019-03314-z.

[12] Pervaiz S, Deiab I, Kishawy H. Hole quality assessment in peck drilling. In: 2012 8th international symposium on mechatronics and its applications. 2012, p. 1–5. http://dx.doi.org/10.1109/ISMA.2012.6215180.

[13] Ravisubramanian S, Shunmugam MS. Investigations into peck drilling process for large aspect ratio microholes in aluminum 6061-T6. Mater Manuf Process 2018;33(9):935–42. http://dx.doi.org/10.1080/10426914.2017.1376076.

[14] Zhaoju Z, Sun X, Guo K, Sun J, Li J. Recent advances in drilling tool temperature: A state-of-the-art review. Chin J Mech Eng 2022;35. http://dx.doi.org/10.1186/s10033-022-00818-w.

[15] Barzegar Z, Ozlu E. Analytical prediction of cutting tool temperature distribution in orthogonal cutting including third deformation zone. J Manuf Process 2021;67:325–44. http://dx.doi.org/10.1016/j.jmapro.2021.05.003, URL: https://www.sciencedirect.com/science/article/pii/S152661252100325X.

[16] Caprino G, Nele L, Santo L, et al. On the origin of cutting forces in machining unidirectional composite materials. In: Proceedings of the 1996 3rd biennial joint conference on engineering systems design and analysis, vol. 75, ASME, New York, NY, United States; 1996, p. 83–7.

[17] Langella A, Nele L, Maio A. A torque and thrust prediction model for drilling of composite materials. Compos Part A: Appl Sci Manuf 2005;36(1):83–93. http://dx.doi.org/10.1016/j.compositesa.2004.06.024, URL: https://www.sciencedirect.com/science/article/pii/S1359835X04001770.

[18] Flachs JR, Salahshoor M, Melkote SN. Mechanistic models of thrust force and torque in step-drilling of al7075-t651. Prod Eng 2014;8:319–33. http://dx.doi.org/10.1007/s11740-014-0531-5.

[19] Oxley PLB, Shaw MC. Mechanics of machining: An analytical approach to assessing machinability. J Appl Mech 1990;57(1). http://dx.doi.org/10.1115/1.2888318, 253–253.

[20] Chandrasekharan V, Kapoor SG, DeVor RE. A mechanistic approach to predicting the cutting forces in drilling: With application to fiber-reinforced composite materials. J Eng Ind 1995;117:559–70. http://dx.doi.org/10.1115/1.2803534.

[21] Guimarães BMP, da Silva Fernandes CM, de Figueiredo DA, da Silva FSCP, Miranda MGM. Cutting temperature measurement and prediction in machining processes: comprehensive review and future perspectives. Int J Adv Manuf Technol 2022;120:2849–78. http://dx.doi.org/10.1007/s00170-022-08957-z.

[22] Strenkowski JS, Hsieh CC, Shih AJ. An analytical finite element technique for predicting thrust force and torque in drilling. Int J Mach Tools Manuf 2004;44:1413–21. http://dx.doi.org/10.1016/j.ijmachtools.2004.01.005, URL: https://www.sciencedirect.com/science/article/pii/S0890695504000082.

[23] Patne HS, Kumar A, Karagadde S, Joshi SS. Modeling of temperature distribution in drilling of titanium. Int J Mech Sci 2017;133:598–610. http://dx.doi.org/10.1016/j.ijmecsci.2017.09.024, URL: https://www.sciencedirect.com/science/article/pii/S0020740317308238.

[24] Segurajauregui U, Arrazola PJ. Heat-flow determination through inverse identification in drilling of aluminium workpieces with MQL. Prod Eng 2015;9:517–26. http://dx.doi.org/10.1007/s11740-015-0631-x.

[25] Fleischer J, Pabst R, Kelemen S. Heat flow simulation for dry machining of power train castings. CIRP Ann 2007;56:117–22. http://dx.doi.org/10.1016/j.cirp.2007.05.030, URL: https://www.sciencedirect.com/science/article/pii/S0007850607000315.

[26] Kumar A, Bhardwaj R, Joshi SS. Thermal analysis of drilling in titanium under flood and cryogenic cooling using coupled CFD and FEM. J Manuf Process 2022;81:605–23. http://dx.doi.org/10.1016/j.jmapro.2022.06.075, URL: https://www.sciencedirect.com/science/article/pii/S1526612522004625.

[27] Lalwani DI, Mehta NK, Jain PK. Extension of oxley's predictive machining theory for johnson and cook flow stress model. J Mater Process Technol 2009;209:5305–12. http://dx.doi.org/10.1016/j.jmatprotec.2009.03.020, URL: https://www.sciencedirect.com/science/article/pii/S0924013609001101.

[28] Minukhin I. An improved method of cutting forces prediction for the primary cutting edges of twist drills. (Master's thesis), Concordia University; 2013, Unpublished. URL: https://spectrum.library.concordia.ca/id/eprint/977065/.

[29] Altintas Y. Manufacturing Automation: Metal Cutting Mechanics, Machine Tool Vibrations, and CNC Design. Cambridge: Cambridge University Press; 2012, http://dx.doi.org/10.1017/CBO9780511843723.

[30] Shi H, Chen Z, Lin X, Zhu T. Accurate temperature characterization and experimental verification in the PCB drilling process. Int J Adv Manuf Technol 2022;120:3507–18. http://dx.doi.org/10.1007/s00170-022-08808-x.

[31] Buss L, Schumski L, Sölter J, Avila K, Karpuschewski B, Fritsching U. Minimum quantity lubrication (MQL) multiphase dynamics of a vibration-assisted drilling process. Procedia CIRP 2023;117:420–5. http://dx.doi.org/10.1016/j.procir.2023.03.071, 19th CIRP Conference on Modeling of Machining Operations. URL: https://www.sciencedirect.com/science/article/pii/S2212827123002032.

[32] Salame C, Bejjani R, Marimuthu P. A better understanding of cryogenic machining using CFD and fem simulation. Procedia CIRP 2019;81:1071–6. http://dx.doi.org/10.1016/j.procir.2019.03.255.

[33] Mohamad Fauzee NF, Abdul Halim NH, Solihin ZH, Tharazi I, Zakaria IA, Hadi MA. A computational fluid dynamics analysis of cryo-CO2 flow and thermal behaviour in high-speed milling process. Appl Therm Eng 2025;264:125342. http://dx.doi.org/10.1016/j.applthermaleng.2024.125342, URL: https://www.sciencedirect.com/science/article/pii/S1359431124030102.

[34] Pelosin M, Albertelli P, Lucchini T. A novel simulation methodology for orthogonal cryogenic machining with CFD spray cooling integration. J Manuf Process 2024;120:61–73. http://dx.doi.org/10.1016/j.jmapro.2024.04.014, URL: https://www.sciencedirect.com/science/article/pii/S1526612524003645.

[35] Yıldız A, Kurt A, Yağmur S. Finite element simulation of drilling operation and theoretical analysis of drill stresses with the deform-3D. Simul Model Pr Theory 2020;104:102153. http://dx.doi.org/10.1016/j.simpat.2020.102153, URL: https://www.sciencedirect.com/science/article/pii/S1569190X20300927.

[36] Li R, Shih AJ. Tool temperature in titanium drilling. J Manuf Sci Eng 2007;129(4):740–9. http://dx.doi.org/10.1115/1.2738120, arXiv:https://asmedigitalcollection.asme.org/manufacturingscience/article-pdf/129/4/740/5510321/740{_}1.pdf.

[37] Fu Z, Yang W, Wang X, Leopold J. Analytical modelling of milling forces for helical end milling based on a predictive machining theory. Procedia CIRP 2015;31:258–63. http://dx.doi.org/10.1016/j.procir.2015.03.013, 15th CIRP Conference on Modelling of Machining Operations (15th CMMO). URL: https://www.sciencedirect.com/science/article/pii/S2212827115002115.

[38] Karaguzel U, Bakkal M, Budak E. Process modeling of turn-milling using analytical approach. Procedia CIRP 2012;4:131–9. http://dx.doi.org/10.1016/j.procir.2012.10.024, 3rd CIRP Conference on Process Machine Interactions. URL: https://www.sciencedirect.com/science/article/pii/S2212827112003150.

[39] Armarego EJA, Brown RH. The machining of metals. Englewood Cliffs: 3826; 1969, OCLC.

[40] Oxley PLB. The mechanics of machining: an analytical approach to assessing machinability. In: Ellis horwood series in mechanical engineering, Chichester: Horwood [u.a.]; 1989.

[41] Lin GCI, Mathew P, Oxley PLB, Watson AR. Predicting cutting forces for oblique machining conditions. Proc Inst Mech Eng 1982;196:141–8. http://dx.doi.org/10.1243/PIME_PROC_1982_196_015_02.

[42] Stabler GV. The Fundamental Geometry of Cutting Tools. Proc Inst Mech Eng 1951;165(1):14–26. http://dx.doi.org/10.1243/PIME_PROC_1951_165_008_02, URL: https://journals.sagepub.com/doi/10.1243/PIME_PROC_1951_165_008_02.

[43] Stabler GV. The chip flow law and its consequences. In: 5th international machine tool design and research conference.. Pergamon, Oxford; 1964, p. 243–51.

[44] Zorev NN. Metal Cutting Mechanics. Oxford: Pergamon Press; 1966.

[45] Russell J, Brown R. The measurement of chip flow direction. Int J Mach Tool Des Res 1966;6(3):129–38. http://dx.doi.org/10.1016/0020-7357(66)90018-7, URL: https://linkinghub.elsevier.com/retrieve/pii/0020735766900187.

[46] Carslaw H, Jaeger J. Conduction of heat in solids. In: Oxford science publications, Clarendon Press; 1959, URL: https://books.google.it/books?id=y20sAAAAYAAJ.

[47] Albertelli P. Energy saving opportunities in direct drive machine tool spindles. J Clean Prod 2017;165:855–73. http://dx.doi.org/10.1016/j.jclepro.2017.07.175, URL: https://linkinghub.elsevier.com/retrieve/pii/S0959652617316219.

[48] Benmeddour A. Experimental investigation and numerical prediction of the effects of cutting tool geometry during turning of AISI-316l steel. Period Polytech Mech Eng 2021;65(4):293–301. http://dx.doi.org/10.3311/PPme.16844, URL: https://pp.bme.hu/me/article/view/16844.

[49] Kim CS. Thermophysical properties of stainless steels. Technical Report, Argonne National Lab., Ill. (USA); 1975, http://dx.doi.org/10.2172/4152287, URL: https://www.osti.gov/biblio/4152287.

[50] Han C, Zhang D, Luo M, Wu B. Chip evacuation force modelling for deep hole drilling with twist drills. Int J Adv Manuf Technol 2018;98(9):3091–103. http://dx.doi.org/10.1007/s00170-018-2488-6.

[51] Zhang A, Zhang S, Bian C, Kong H. Modified chip-evacuation force modeling and chip-clogging prediction in drilling of cortical bone. IEEE Access 2019;7:180671–83. http://dx.doi.org/10.1109/ACCESS.2019.2958428.

[52] Priest J, Ghadbeigi H, Avar-Soberanis S, Gerardis S. 3D finite element modelling of drilling: The effect of modelling method. CIRP J Manuf Sci Technol 2021;35:158–68. http://dx.doi.org/10.1016/j.cirpj.2021.06.001, URL: https://www.sciencedirect.com/science/article/pii/S1755581721000912.

[53] Cardiff P, Batistiq. Solids4foam: A toolbox for performing solid mechanics and fluid-solid interaction simulations in openfoam. J Open Source Softw 2025;10(108):7407. http://dx.doi.org/10.21105/joss.07407.